Pure and Applied Geophysics

Inversion of Magnetic Data Acquired with a Rotary-Wing Unmanned Aircraft System for Gold Exploration

MICHAEL CUNNINGHAM,[1] CLAIRE SAMSON,[1] JEREMY LALIBERTÉ,[2] MARK GOLDIE,[3] ALAN WOOD,[4] and
DAVID BIRKETT[4]

Abstract—A hexacopter unmanned aircraft system instrumented with a caesium vapour magnetometer recorded total magnetic intensity over a 5.0 km^2 prospective gold area in the Abitibi Subprovince of the Canadian Precambrian Shield. The survey also included a N–S repeatability line which showed that the unmanned aircraft system was very stable in flight with average standard deviations from nominal altitude and easting being 1.8 m and 0.7 m, respectively. The total magnetic intensity map revealed the structural framework of the banded iron formations present in the survey area and showed that the gold ore zones are not directly associated with magnetic highs but rather with steeply dipping faults. The total magnetic intensity data was inverted in 3-D using unconstrained and constrained approaches with 12.5 m (northing) × 12.5 m (easting) × 5 m (depth) cells and a maximum of 20 iterations. The processed (after diurnal corrections, heading correction, and tie-line levelling) total magnetic intensity data was input directly in the unconstrained inversion algorithm. Initial model building for the constrained inversion was a much more laborious process involving the inclusion of 15 synthetic structures based on borehole magnetic susceptibility measurements and knowledge of the local geology. The results of both inversion approaches were very similar. They revealed the presence of near-vertical thin sheets, individually resolvable down to approximately 400 m. In this particular case, the straightforward unconstrained inversion yielded a realistic and detailed model of the subsurface in approximately 1 h of runtime. Unmanned aircraft system total magnetic intensity data could therefore be processed and inverted almost immediately after acquisition and have an impact on decisions made in the field while a survey is still in progress.

Keywords: Unmanned aircraft systems, Magnetics, Inversion, Airborne surveying, Mineral exploration.

1. Introduction

With the rapid technological development of unmanned aircraft systems (UAS) over the past decade, UAS are an alternative to conventional aircraft for numerous applications (e.g. photography, surveillance, site inspection, and geophysical surveying). UASs have become a valuable option within the mineral exploration industry as an aeromagnetic survey platform. They are capable of providing high-quality and high-resolution data by flying slower, at lower altitudes, and with improved maneuverability than traditional platforms. Moreover, they can fly during the day and at night, in jurisdictions where it is permitted, with no risk of pilot fatigue or injury.

Recent research has primarily focused on demonstrating the capabilities of different aeromagnetic survey systems (Cunningham et al. 2017; Parvar et al. 2018; Pei et al. 2017; Walter 2019a; Wood et al. 2016), as well as quantifying and reducing noise levels (Huq, Forrester, and Ahmadi 2015; Sterligov and Cherkasov 2016; Tuck et al. 2018, 2019; Walter et al. 2019b, c).

Aeromagnetic surveying with UASs is primarily performed using a single rotor helicopter or multi-rotor style unmanned aircraft (Cunningham et al. 2017; Malehmir et al. 2017; Parshin et al. 2018; Parvar et al. 2018; Sterligov et al. 2018; Stoll 2013; Tuck et al. 2019; Walter et al. 2019a) with only a few exceptions (Cherkasov et al. 2016; Wood et al. 2016). Helicopter and multi-rotor UASs typically use a single magnetic sensor either mounted rigidly to the platform or hanging beneath it. Although each strategy has its own potential drawback (e.g. data acquired with a rigidly mounted sensor is mostly

[1] Department of Earth Sciences, Carleton University, 1125 Colonel By Drive, Ottawa, ON K1S 5B6, Canada. E-mail: michael.cunningham@carleton.ca
[2] Department of Mechanical and Aerospace Engineering, Carleton University, 1125 Colonel By Drive, Ottawa, ON K1S 5B6, Canada.
[3] IAMGOLD Corporation, 401 Bay St #3200, Toronto, ON M5H 2Y4, Canada.
[4] Stratus Aeronautics, #123, 3191 Thunderbird Crescent, Burnaby, BC V5A 3G1, Canada.

affected by vibrational noise whereas data acquired with a hanging sensor suffers mostly from rotational noise), UASs have been demonstrated to provide high-quality data, such that their fourth difference noise levels are within the airborne industry standard (0.1 nT) (Coyle et al. 2014).

Total magnetic intensity (TMI) and gradiometric results from aeromagnetic surveys can give insight into the geological subsurface, terrain and structure (Dentith and Mudge 2014). Furthermore, using magnetic data inversion, a greater understanding of constraints can be achieved (Vallée et al. 2019). The objective of this paper is to demonstrate how UAS aeromagnetic data that was acquired above tree canopy [50 m above ground level (AGL)] in the boreal forest, near Chibougamau, Quebec, Canada, can be successfully inverted in three dimensions (3-D), with a minimum amount of pre-processing and constraints, to yield a realistic model of the subsurface in support of gold exploration. This paper includes unconstrained and constrained inversion models over a prospective region and provides commentary into the added benefit of inverting UAS aeromagnetic data.

2. Geology of the Survey Area

The survey area is a section of the Nelligan property (Fig. 1), owned by IAMGOLD Corporation and Vanstar Mining Resources. The property is located approximately 55 km southwest of Chibouganau, Quebec, Canada in the Abitibi Subprovince of the Late Archean Superior Province of the Canadian Precambrian Shield. The Abitibi Subprovince extends for 500 km from east to west and is bounded by the Grenville Province (east), Wawa Sub Province (west), Quetico and Opatica Subprovinces (north) and the Pontiac Subprovince (south). The Abitibi Subprovince is composed of east-trending synclines of primarily volcanic rocks and intruding domes with synvolcanic and/or syntectonic plutonic rock cores (Daigneault et al. 2004). Primary rock compositions include gabbro-diorite, tonalite, and granite. Most of the strata (volcanic and sedimentary) are vertically dipping and separated by eastward trending faults of variable dips.

Figure 1 ►
Location and geological maps. Top: Eastern Canada overview. Middle: regional map. Bottom: Local geological map adapted from Carrier et al. (2019) and SIGEOM (2020). Base map source: ESRI, HERE, Garmin

More precisely, the Nelligan property is located within the Caopatina-Desmaraisville segment of the Abitibi Subprovince which features four groups of faults based on their direction (ordered from oldest to youngest): E–W, S–E, N–E, and NNE (Carrier et al. 2019). The E–W and S–E faults are related to the primary episode of deformation, while the N–E faults cut regional schistocity and the E–W faults and the NNE faults are related to Grenvillian orogeny. The Caopatina-Desmaraisville segment is primarily composed of volcanic rocks from the Deloro Assemblage (2734–2724 Ma) where several volcanic cycles have occurred (Carrier et al. 2019; Chown et al. 1991).

The Nelligan property is centered on an E–W syncline bounded to the north and south by the Obatogamau Formation volcanic rocks. Diamond borehole data has determined that the local geology is composed of strongly altered sedimentary rocks hosted in the Caopatina formation sediments (Carrier et al. 2019) belonging to the North Volcanic Zone of the Abitibi Subprovince. There are several preserved folding events oriented N–S to NNW in the Nelligan property. The main deformation occurred following these folds. This deformation is primarily characterized by N–S regional shortening (Carrier et al. 2019) and is the origin of the E–W tectonic structure identified by: large fold axes; regional schistosity (E–W trending); and longitudinal faults. This deformation is followed by a deformation episode causing shear cleavages that cut or fold the main regional schistosity or crenulation cleavages affecting regional schistosity (Chown et al. 1991). The northern region of the Nelligan property also contains numerous regional and local structures and deformation zones, and hosts granodioritic to tonalitic intrusions. Previous exploration efforts (VTEM; ground magnetics; helicopter-borne magnetics; and borehole data) has allowed for the identification and inference of deformed segments of banded iron formation (BIF).
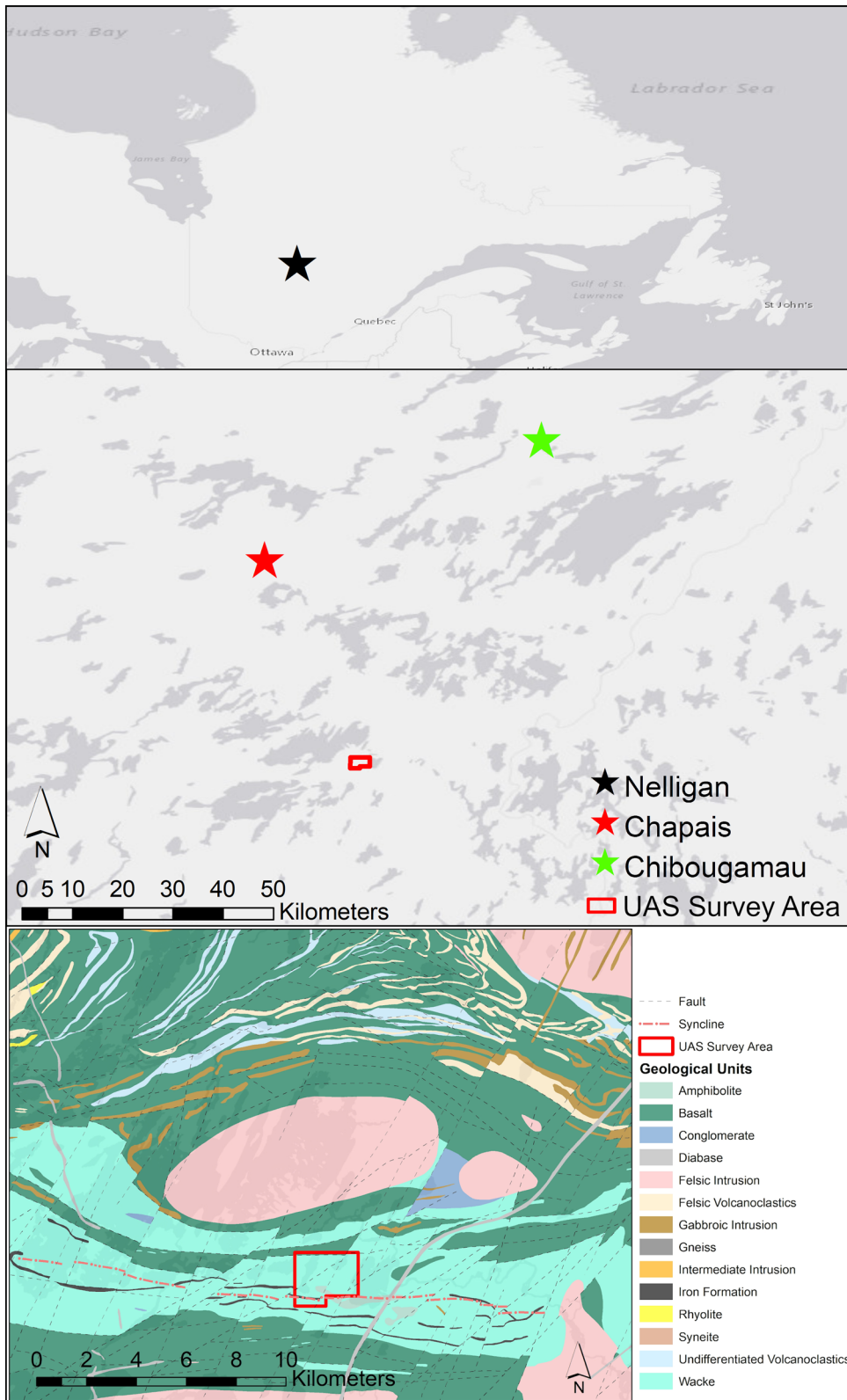
The Nelligan property has atypical gold mineralization for Abitibi type deposits, as it is hosted in sedimentary basins, more specifically in the sedimentary rocks of the Caopatina Formation, which overlay earlier volcanic cycles. These sedimentary rocks are composed of feldspathic wacke, turbidites, greywackes, conglomerates, and iron formation layers. Furthermore, there are basalts and gabbro sills interwoven between beddings. The property contains four different known gold mineralization zones grouped by their mineralization style (Fig. 2):

- *Renard Zone*: Silicified units with phlogopite zones (length: 1100+ m; width: 150–250 m);
- *Zone 36*: Silicified zones in the east, and silicified and hematized tectonic breccias in the west (length: 200–300 m; width: 5–10 m);

- *Liam Zone*: Schists and silicified zones with pseudo iron formations (length: 700 m; width: 20–30 m);
- *Dan Zone*: Silicified and hematized isolated conglomerate lenses (length: 300-500 m; width: 10–20 m).

The mineralization zones are generally located at the boundary between upper greenschist and amphibolite facies and are adjacent to first-order crustal faults.

The Nelligan property contains overburden between 10 and 50 m in thickness. There are no known outcrops, making geophysics a very important aspect of mineral exploration. The topography is generally flat with some rolling hills; there is a total elevation change of less than 40 m over the survey area (Fig. 2).
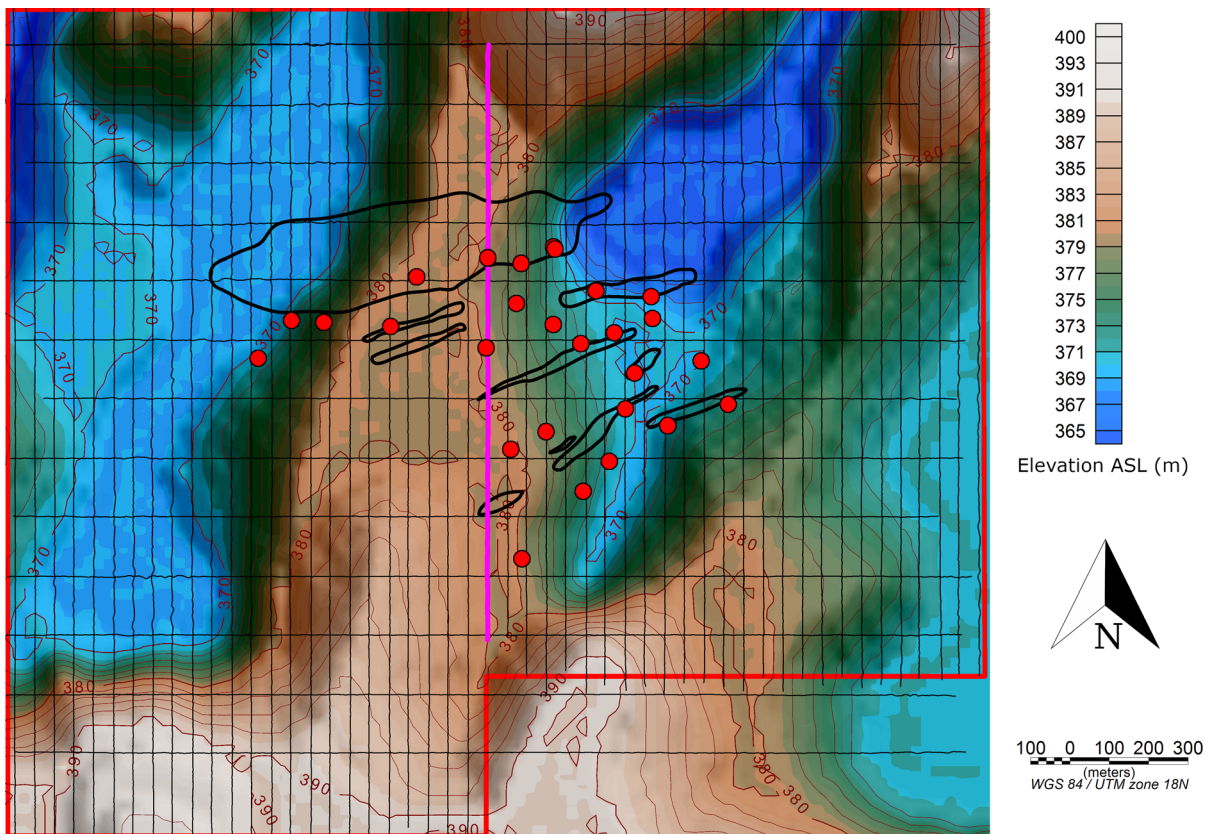

Figure 2
UAS survey area digital elevation (ASL) map. Brown lines are elevation contours at 2 m increments. Black lines are flight lines (traverse lines are oriented north–south, tie lines are oriented east–west). The pink line is the repeatability test flight line (Fig. 4). Black encircled regions highlight known gold ore zones. Red points represent borehole collars

3. UAS Survey

3.1. Description of the Rotary-Wing UAS

The SkyLance 6200, developed by Stratus Aeronautics Inc., is an updated version of the original SkyLance described in Cunningham et al. (2017). It is a prototype hexacopter UAS with a magnetometer front-mounted on a non-magnetically susceptible boom to minimize the magnetic interference from the UAS frame on the sensor data (Fig. 3 and Table 1). It employs six motors mounted on radially orientated arms to ensure stable flight. Avionics include an autopilot system, a differential RTK GPS, radio link for streaming data, and a barometric altimeter for altitude above sea level (ASL) measurements. The main payload is a Geometrics G-823A caesium vapour magnetometer, which records scalar aeromagnetic data at a frequency of 10 Hz.

3.2. UAS Flights

The SkyLance 6200 UAS performed flights between September 29, 2019 and October 3, 2019.

Table 1

Specifications of the SkyLance 6200 UAS

UAS type	Hexacopter
Crew size	3
Total mass	$\approx$ 15 kg (excluding payload)
Payload mass	5 kg
Endurance	30 min at 32 km/h
Maximum flight speed	37 km/h
Sensor	Geometrics G-823A caesium vapour magnetometer

During the UAS survey it was partially cloudy, with temperatures ranging between − 1 °C to + 7 °C, and wind speeds between 5 and 30 km/h. Space Weather Canada reported quiet to unsettled solar activity for the sub-auroral zone where the survey was located; minimal magnetic noise would be due from solar activity.

Over the UAS survey area a total of 319.7 line-km were flown; however, for this study only a total of 131.5 line-km was considered. Figure 2 shows the 50 traverse lines flown at a 50 m line spacing with a N–S heading (97.7 line-km) and the 14 tie lines flown at a

Figure 3
Stratus Aeronautics SkyLance 6200

150 m line spacing with a E–W heading (33.8 line-km). To ensure the UAS flew safely above the trees and to ensure visual line of sight operations, the survey grid was flown at a nominal altitude of 50 m AGL (395 m ASL). The UAS flew at a speed of approximately 38 km/h. Since the sampling frequency of the magnetometer is 10 Hz, this corresponds to a spatial sampling interval of approximately 1 data point per metre.

The pink line in Fig. 2 was flown four times at three nominal flight altitudes to assess repeatability, 395 m, 400 m, and 405 m ASL. The 405 m line was flown twice for direct altitude comparison. The TMI variation (top left), altitude variation (bottom left), and flight line positional variation (right) are presented in Fig. 4 and summarised in Table 2. The mean altitudes (ASL) for each flight were all within 1.8 m of their nominal altitudes. Altitude variations
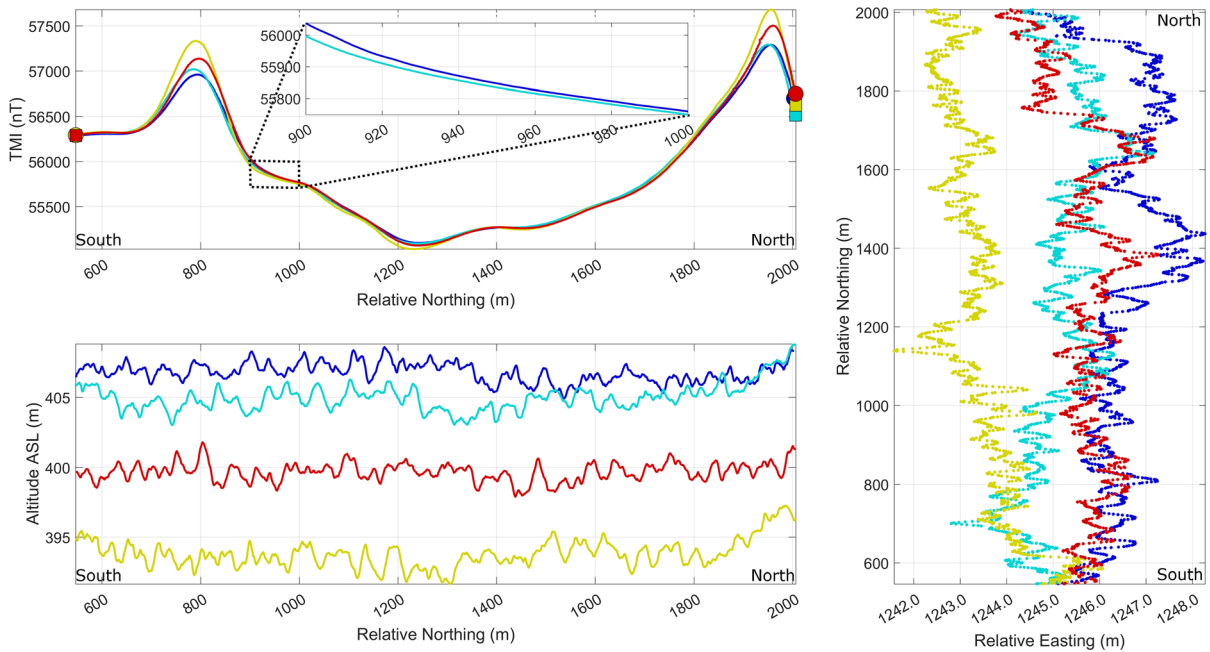

Figure 4
Repeatability flights along a single survey line (pink line in Fig. 2). Top left—magnetic intensity variation for each flight with focussed region for direct comparison between 405 m nominal altitude flights; Bottom left—flight altitude for each of the flights; and right—positional variation along the flight lines. Each colour [dark blue (1), light blue (2), red (3), and yellow (4)] represent different flights. The dark and light blue flights were flown at a nominal altitude of 405 m, the red flight at a nominal altitude of 400 m, and the yellowflight at a nominal altitude of 395 m

Table 2

Variation from nominal altitude ASL and easting for the four flights along the repeatability flight line (Fig. 2)

Repeatability Line	Heading	Altitude ASL (m)					Deviation from nominal easting (m)				
		Nominal	Mean	Maximum	Minimum	Standard deviation	Nominal	Mean	Maximum	Minimum	Standard deviation
1	North	405.0	406.8	408.6	404.9	0.7	0.0	1.6	3.3	− 0.6	0.7
2	South	405.0	405.0	408.8	403.0	1.0	0.0	0.2	2.2	− 2.2	0.7
3	South	400.0	399.7	401.8	397.9	0.6	0.0	0.7	2.3	− 1.2	0.7
4	North	395.0	393.8	397.3	391.7	1.0	0.0	− 1.6	1.1	− 3.4	0.7

had a total range of 5.8 m or less (ASL), and an average standard deviation of 0.8 m. The mean eastings for each flight were within 1.6 m from their nominal eastings; variations had a total range of 4.5 m or less, and an average standard deviation of 0.7 m. Data from flights with a south heading showed less altitude variation, but no significant change in easting variation was observed, suggesting that wind was from the north to the south, and caused minimal effects on flight.

The residual magnetic intensity (RMI) map from the UAS survey area is presented in Fig. 5; processing included diurnal correction, heading correction, and tie-line levelling. Minimum curvature interpolation at ¼ the flight line spacing (Lee and Morris 2013) was applied as part of standard practice, producing a cell size of 12.5 m × 12.5 m using Geosoft's Oasis Montaj. The four gold ore zones are circled in black. Magnetic highs do not coincide with the gold ore zones; instead the highs are related to BIFs and give insight into the structural framework of the area.

4. 3-D Inversion

Inversion, also known as inverse modelling, is an automated, iterative, modelling process that employs computer algorithms to create a model of a geophysical property by linking observation and a computed response (Dentith and Mudge 2014, Walker 2018). The 'goodness of fit' between the model and observed response is described by an objective function, where inversion is tasked to iteratively adjust model parameters to minimize this objective function. Inversion can be run either unconstrained or constrained, where unconstrained
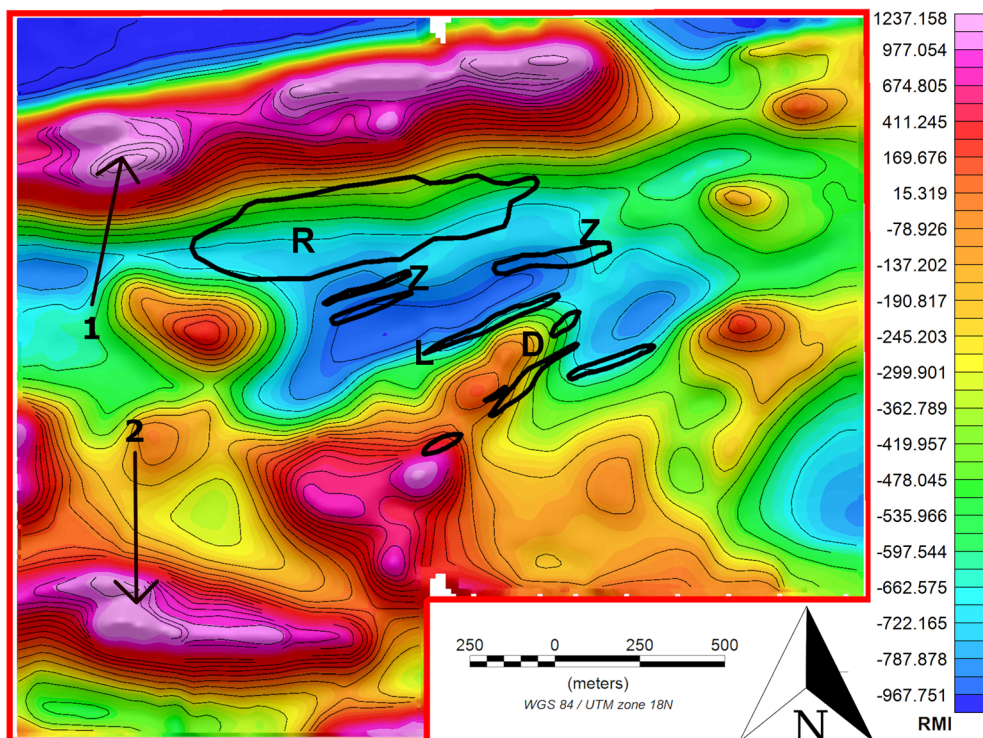

Figure 5
RMI map of the UAS survey area. Black lines outline known gold ore zones: *R* Renard; *Z* Zone 36; *L* Liam; and *D* Dan. Arrows point to east–west trending structures: (1) two discontinuous linear structures producing a high magnetic anomaly along the northern edge of the survey area; and (2) two linear structures that are slightly offset in northing, potentially from structurally deformed BIFs, along the southern edge of the survey area. Contours are every 100 nT

inversion is simpler, as it involves no operator input and is allowed to converge at whichever model best fits the problem. Constrained inversion requires an input of constraints such as surrounding geology, borehole data, and data from other geophysical techniques to limit the possibilities of solutions. This additional information steers the constrained inversion process towards a more realistic model of the subsurface than the unconstrained inversion and assists in avoiding the non-uniqueness problem, a well-known (ill-posed) issue, where there are infinite possibilities that can fit the data.

The RMI data (Fig. 5) was inverted in 3-D using both (1) unconstrained and (2) constrained inversion to yield magnetic susceptibility models of the subsurface. Both unconstrained and constrained inversion were performed using Geosoft's Oasis Montaj and the VOXI toolbox which uses Geosoft's cloud-powered computing. A summary of the inversion parameters is provided in Table 3. The cell size used (12.5 m × 12.5 m × 5 m) for inversion corresponded to a 1:1 cell to data point ratio from the input grid (the RMI map was interpolated to a 12.5 m × 12.5 m cell size). This cell size was chosen as it was the closest match to the number of data points. Other cell sizes were tested (10 m × 10 m × 5 m; 20 m × 20 m × 10 m; and 25 m × 25 m × 10 m) and led to similar results, although fine details started to get lost as the cell size

increased. The error in the inversion is quantified by calculating the root mean square deviation between the observed and calculated data. Inversions were limited to 20 iterations or until a VOXI default fit error of under 5% of the standard deviation of the magnetic data, or 27.4 nT, was achieved. Both constrained and unconstrained inversions were completed before the reaching the 20-iteration limit. They were completed in approximately 1–3 h of runtime through cloud computing using Windows Azure.

4.1. Unconstrained

The unconstrained inversion used the RMI data (Fig. 5) and the digital elevation model of the survey area (Fig. 2). Figure 6 presents horizontal slices through the unconstrained magnetic susceptibility model at various depths. Figure 7 shows vertical slices (labeled in Fig. 6) through the unconstrained magnetic susceptibility model.

4.2. Constrained

Constrained inversion included borehole magnetic susceptibility data and geological knowledge of the area.

Figure 2 shows surface locations of the 27 borehole collars used for the constrained inversion. The spatial distribution of the collars reveals that drilling took place with a primary focus on intersecting gold ore zones. Figure 8 shows the 8.4 km of boreholes with magnetic susceptibility data plotted in 3-D (easting, northing, and depth). Magnetic susceptibility measurements were made using a handheld Terraplus SM-30 magnetic susceptibility meter approximately every 3 m along each core. Susceptibility values ranged from 0 to 550 SI with a mean, median, and standard deviation of 7 SI, 0.2 SI and 23 SI, respectively. Borehole data was used to create a parameter reference model and a parameter weighting model using Oasis Montaj VOXI; a radius around boreholes of 20 m, a weight attenuation factor of 0.1, and a weight minimum threshold of 0.0001 were used.

A modelling tool was developed in MATLAB to create synthetic geological structures and import

Table 3

Inversion parameters for both unconstrained and constrained inversion. IGRF – international geomagnetic reference field

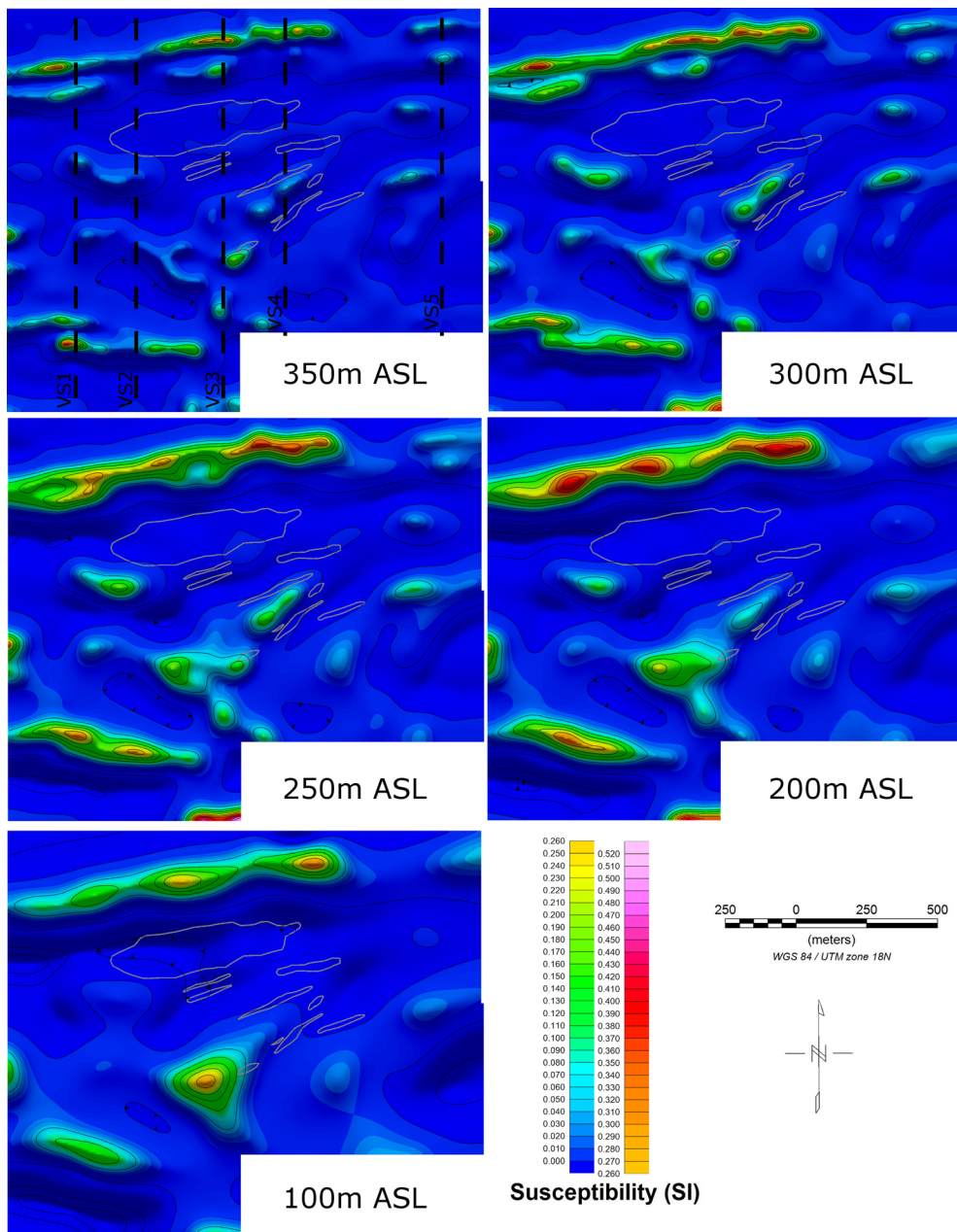| Type of data	RMI
Cell size (m)	x (northing) = 10
	y (easting) = 10
	z (depth) = 5
Maximum number of iterations	20
Minimum fit error (nT)	27.42
IGRF date (dd/mm/yyy)	01/10/2018
IGRF field strength (nT)	55,298
IGRF inclination (degree)	73.0
IGRF declination (degree)	− 15.2
Unconstrained root mean square deviation (nT)	3.30
Constrained root mean square deviation (nT)	1.15

Figure 6

Unconstrained inversion results. Horizontal slices through the 3-D magnetic susceptibility model at various depths as indicated in the bottom right corners. The grey outlines are the known gold ore zones. The black dashed lines correspond to the vertical slices presented in Fig. 7. Contours are every 0.1 SI

them into the initial model (Fig. 9). The tool is capable of modelling 3-D sheet structures with the following parameters: easting, northing, limiting depth, horizontal and vertical lengths, thickness,

strike, dip, and magnetic susceptibility. Table 4 lists the parameters used to describe each of the 3-D sheet structures which were inferred from the RMI map (Fig. 5). For easting, northing, and depth there is a
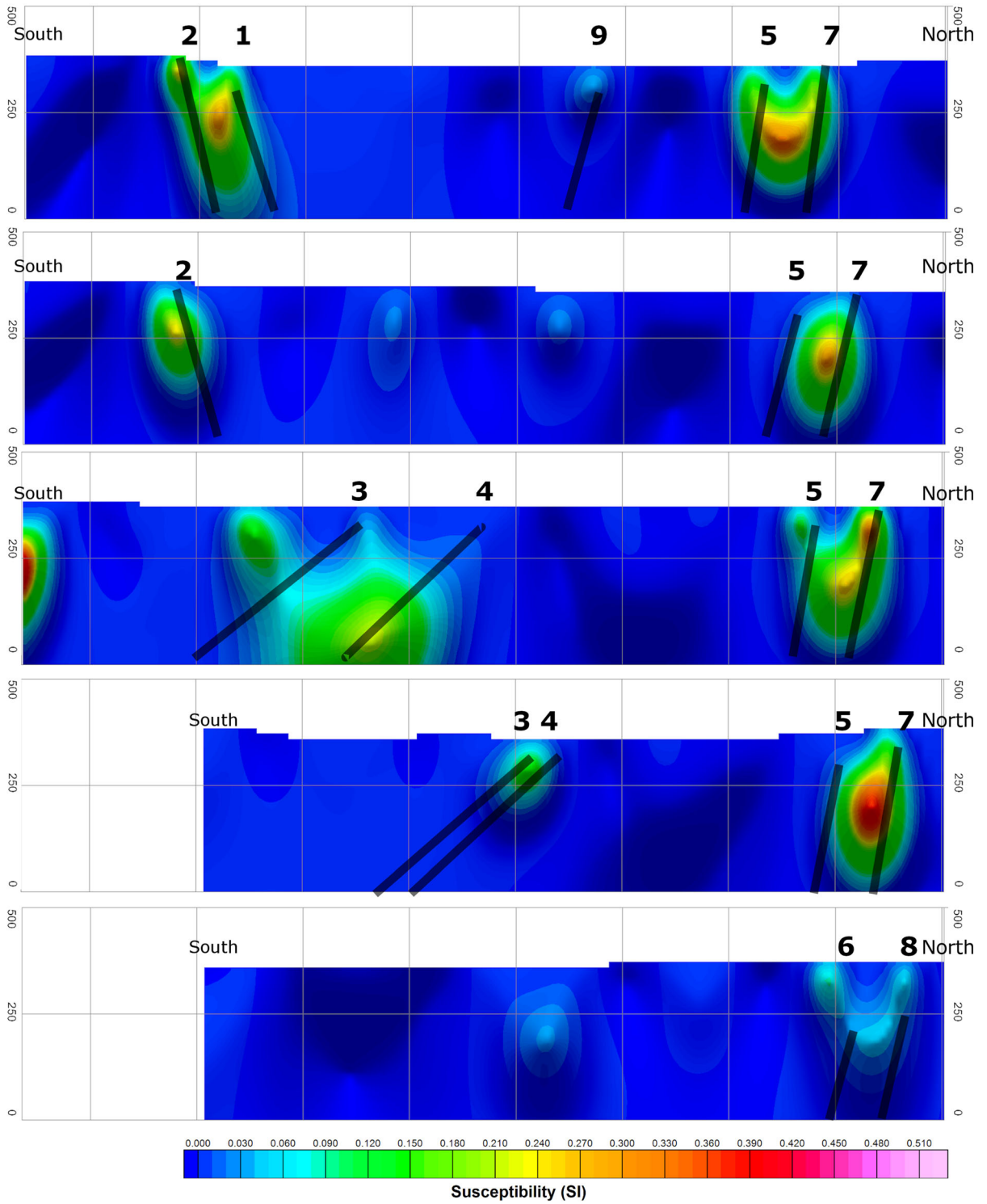
Figure 7
Unconstrained inversion results. Vertical slices through the 3-D magnetic susceptibility model corresponding to the dashed lines drawn on Fig. 6. Solid lines show the traces of the sheet structures and associated numbers (Fig. 9 and Table 4)
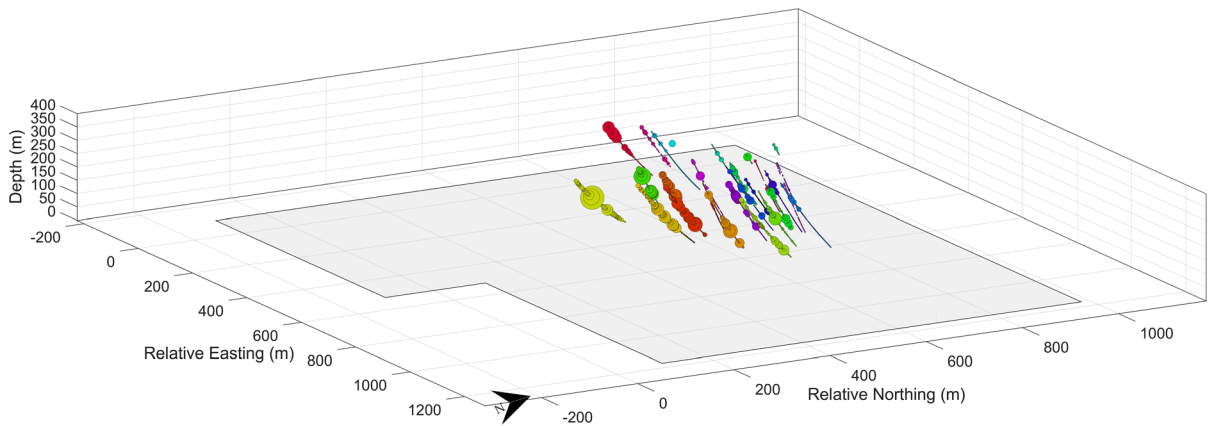
Figure 8
Magnetic susceptibility data from 27 boreholes. Circle size is proportional to the magnetic susceptibility value and range from 0 to 550 SI
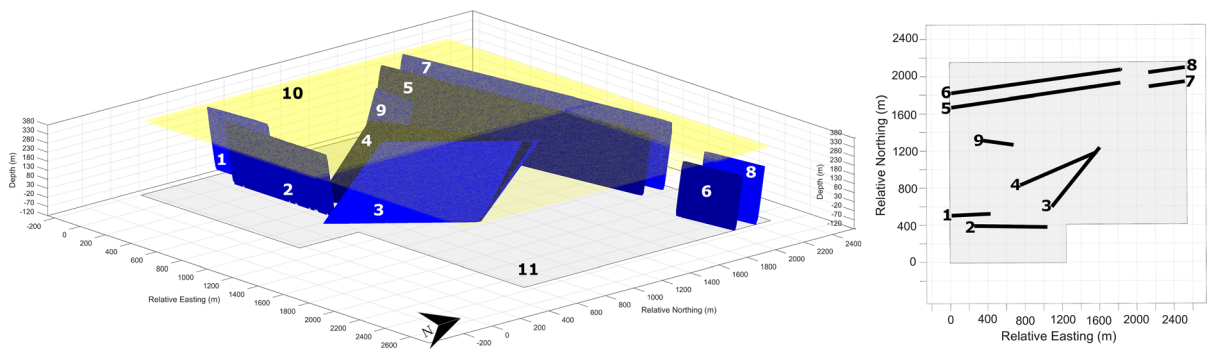

Figure 9
Synthetic geological structures numbered and further described in Table 4. Left—3-dimensional view. Right—map view at 250 m ASL

Table 4

Parameters describing the 3-D structures used for the constrained inversion

| Geological Structure	Figure 8 Structure #	Relative easting (m)			Relative northing (m)			Depth (m)		Strike (°)	Dip (°)	Thickness (m)	Susceptibility (SI)
		Reference	Start	Stop	Reference	Start	Stop	Reference	Limiting				
Sheet 1	1	13		440	448			20	20	265	85	25	10
Sheet 2	2	245	245	1045	347			20	20	270	85	20	10
Sheet 3	3	1195	1075	1605	843			60	20	40	70	20	10
Sheet 4	4	1568	745	1610	1316			20	20	66	65	20	10
Sheet 5	5	22		1837	1700			20	50	82	85	20	10
Sheet 6	6	1919	2137		1838			300	120	82	85	20	10
Sheet 7	7	22		1837	1846			20	20	82	85	20	10
Sheet 8	8	1947	2137		1994			300	100	82	85	20	10
Sheet 9	9	375	345	675	1335	0		20	20	95	80	20	10
Overburden 1	10	852	1359		809		1755	0	0	0	0	10	0.1
Overburden 2	10	852		1359	809			0	0	0	0	20	0.1
Overburden 3	10	852	1359		809	1755		0	0	0	0	20	0.1
Basement	11	852			809			200	200	0	0		1
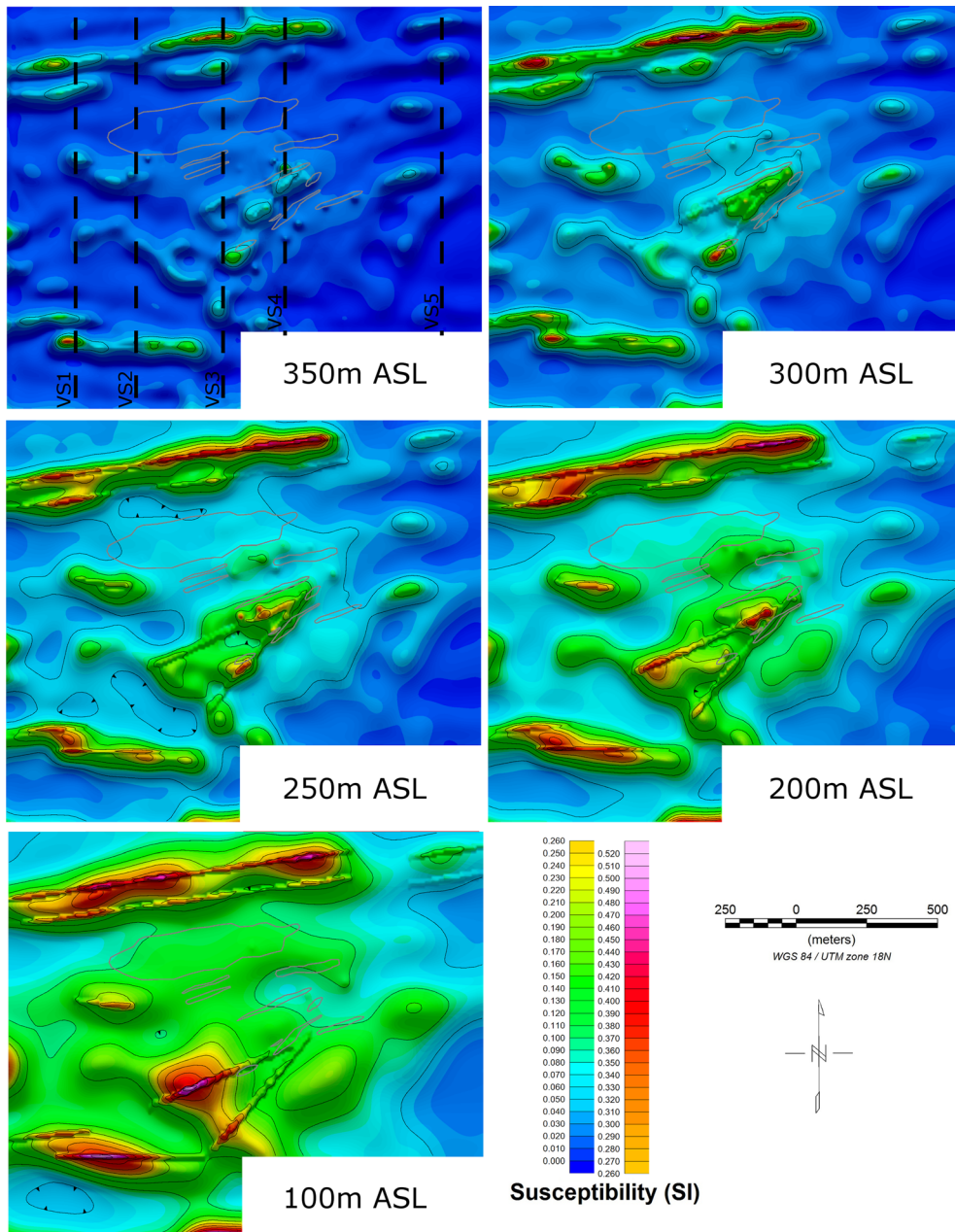
Figure 10
Constrained inversion results. Horizontal slices through the 3-D magnetic susceptibility model at various depths as indicated in the bottom right corners. The grey outlines are the known gold ore zones. The black dashed lines correspond to the vertical slices presented in Fig. 11. Contours are every 0.1SI

reference position, a known or interpreted location where the structure is built from. There are also minimum and maximum limits to the structure's extent (east/west and north/south) and depth. For this

constrained inversion, the reference position is based on interpretation of magnetic data and grids as well as borehole cross-sections. These geological structures (Fig. 9) are converted to voxel models in Oasis
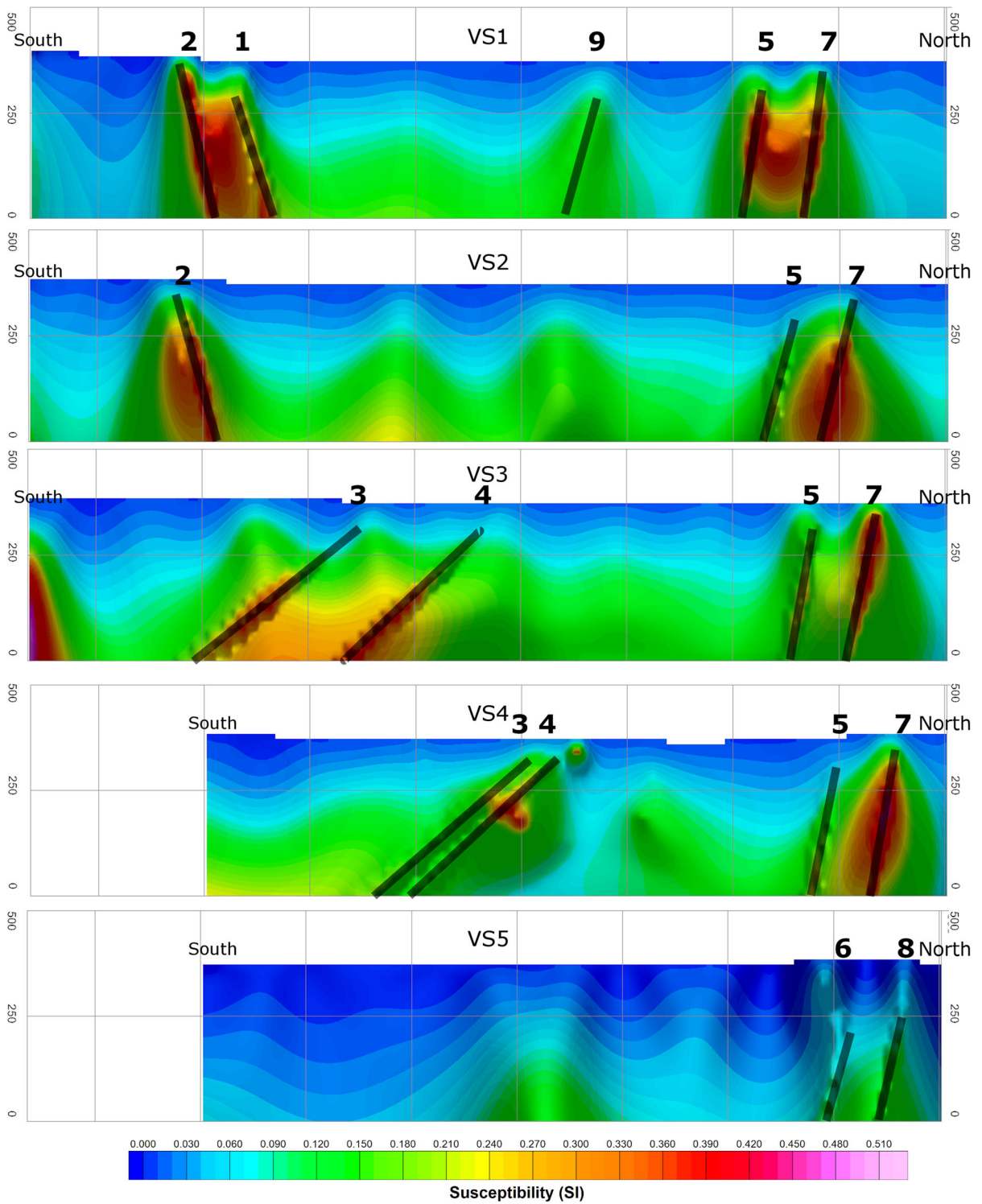
Figure 11
Constrained inversion results. Vertical slices through the 3-D magnetic susceptibility model corresponding to the dashed lines drawn on Fig. 10. Solid lines show the traces of the sheet structures and associated numbers (Fig. 8 and Table 4)

Montaj and then imported in the VOXI inversion toolbox. To account for varying overburden thickness three separate structures were created: sheet 1 is only 10 m thick, extends from the south-east edge of the survey area to 350 m west of that edge, and ends 300 m from the northern edge of the survey area; sheet 2 and sheet 3 are set to 20 m of overburden and fill the rest of the survey area. A map view of the resulting voxel is shown in Fig. 9 (right) at an altitude of 250 m ASL.

The results of the constrained inversion, using the same parameters as for the unconstrained inversion (Table 3) and incorporating steeply dipping structures (Table 4) and the borehole magnetic susceptibility data (Fig. 8) are shown in Figs. 10 and 11.

4.3. Comparison

Both the unconstrained and constrained inversion results are consistent with structural trends by revealing near-vertical structures or thin sheets steeply dipping towards the north and south as shown when projecting synthetic sheet structures (Table 4) into vertical slices through the magnetic susceptibility models (Figs. 7 and 11). The presence of BIFs whom by their nature are typically associated with well-defined linear magnetic anomalies has produced a signature which highlights particularly well the local structural framework. The northern region of the survey area is modelled as two linear sheets trending east–west and steeply dipping southward (structures 5 and 7), down to depths of approximately 400 m beyond which these features are no longer resolvable as two separate structures. The south-western region of the survey area is also modeled as near-vertical sheets down to approximately 400 m but dipping northward (structures 1 and 2). The central region of the survey area is more complicated; there is evidence that both faulting and folding has occurred; the two sheets appear to be dipping south-eastward (structures 3 and 4).

At shallow depths (down to 150 m AGL), the constrained inversion (Fig. 10) provides more structural details than the unconstrained inversion (Fig. 6) (in the 350 m and 300 m ASL maps). On the other hand, near vertical structures appear to blend at shallower depths for the constrained inversion

(Fig. 11) than for unconstrained inversion (Fig. 7). The unconstrained inversion returned magnetic susceptibility values from − 0.144 to 0.569 SI, while the constrained inversion returned values within a similar range between − 0.002 and 0.523 SI.

Typical iron formation units range in magnetic susceptibility from 10^{-2} to 10^2 SI (Clark 1997) depending on the formation's haematite versus magnetite content (Dentith and Mudge 2014). Taner and Chemam (2015) modelled an iron formation, located 250 km west of the Nelligan property, using 0.6 SI. The difference in magnetic susceptibility between the iron formations at these two locations could be due to varying magnetite content. Taner and Chemam (2015) report between 77 and 89% of the iron oxide minerals being magnetite with the rest primarily being haematite. The iron formations found on the Nelligan property contain centimetric alternations of magnetite and haematite bands but there is no data on the relative abundance of the two minerals.

5. Discussion and Conclusion

A key finding of this study is the similarity between the results of the unconstrained and constrained inversion. The initial model of the constrained inversion, a laborious process, incorporated 13 modelled structures, magnetic susceptibility data from 27 boreholes totalling 8.4 km spaced every 3 m to steer the results towards a model of the subsurface consistent with a priori knowledge of the geology of the survey area. On the other hand, the straightforward unconstrained inversion which simply inputs the processed TMI data gives a detailed model of the subsurface and the results are not biased towards any preconceived interpretation of the local geology. The convergence of the unconstrained inversion towards a realistic model of the subsurface is attributable to the high density (approximately 12 data points per 12.5 m × 12.5 cell) and high quality [as demonstrated by repeatability statistics (Table 2)] both, in turn, being related to the capability of the UAS of flying at low speed in a stable manner.

The minimal data handling required for unconstrained inversion of TMI data acquired by a UAS and the relatively short time needed to run an

inversion (approximately 1 h) makes it possible to envisage that TMI data could be processed and inverted almost immediately after it has been acquired, while the survey team is still in the field. A quick interpretation of the results could impact the continuation of the survey in the following days (e.g. flying lines with tighter spacing over areas of particular exploration interest or perpendicular to the strike of newly identified structures). The results of this research project reinforce the fact that UAS magnetometry has now reached a level of technical maturity such that it has become a useful operational tool for gold mineral exploration surveys.

References

Carrier, A., Nadeau-Benoit, V., & Faure, S. (2019). NI 43-101 Technical report and initial mineral resource estimate for the Nelligan Project, Quebec, Canada. Accessed 08–01–2020, https://vanstarmining.com/wp-content/uploads/2019/12/IAMGOLD_VANSTAR_43-101_FINAL.pdf.

Cherkasov, S., Sterligov, B., & Zolotaya, L. (2016). On the use of unmanned aerial vehicles for high-precision measurements of the Earth's magnetic field. *Moscow University Geological Bulletin., 71*(4), 296–299. https://doi.org/10.3103/S0145875216040037.

Chown, E. H., Daigneault, R., & Mueller, W. (1991). Part 1: geological Setting of the eastern Extremity of the Abitibi Belt. In: 8th IAGOD Symposium, Ottawa, Ontario; CA; August 12–18, 1990. https://doi.org/10.4095/132277

Clark, D. A. (1997). Magnetic petrophysics and magnetic petrology: aids to geological interpretation of magnetic surveys. *AGSO Journal of Australian Geology and Geophysics, 17*(2), 83–103.

Coyle, M., Dumont, R., Keating, P., Kiss, F., & Miles, W. (2014). Aeromagnetic surveys: Design, quality assurance, and data dissemination. *Geological Survey of Canada Open File, 7660,* 48. https://doi.org/10.4095/295088 (**Pei 2017**).

Cunningham, M., Samson, C., Wood, A., & Cook, I. (2018). Aeromagnetic surveying with a rotary-wing unmanned aircraft system: a case study from a zinc deposit in Nash Creek, New Brunswick Canada. *Pure and Applied Geophysics., 175,* 3145–3158.

Daigneault, R., Mueller, W. U., & Chown, E. H. (2004). Abitibi greenstone belt plate tectonics: the diachronous history of arc development, accretion and collision. In P. G. Eriksson, W. Altermann, D. R. Nelson, W. U. Mueller, & O. Catuneanu (Eds.), *The Precambrian earth: tempos and events, series: developments in Precambrian geology* (Vol. 12, pp. 88–103). Amsterdam: Elsevier.

Dentith, M., & Mudge, S. T. (2014). *Geophysics for the mineral exploration geoscientist*. Cambridge: University Press.

Huq, M., Forrester, R., & Ahmadi, M. (2015). Magnetic characterization of actuators for an unmanned aerial vehicle. *IEEE/ASME Transactions on Mechatronics., 20*(4), 1986–1991.

Lee, M., & Morris, W. (2013). Quality assurance of aeromagnetic data using lineament analysis. *Exploration Geophysics, 44,* 104–113.

Malehmir, A., Dynesius, L., Paulusson, K., Paulusson, A., Johansson, H., Bastani, M., et al. (2017). The potential of rotary-wing UAV-based magnetic surveys for mineral exploration: A case study from central Sweden. *Leading Edge, 36*(7), 552–557. https://doi.org/10.1190/tle36070552.1.

Parshin, A., Morozov, V., Blinov, A., Kosterev, A., & Budyak, A. (2018). Low-altitude geophysical magnetic prospecting based on multirotor UAV as a promising replacement for traditional ground survey. *Geo-spatial Information Science, 21*(1), 67–74. https://doi.org/10.1080/10095020.2017.1420508.

Parvar, K., Braun, A., Layton-Matthews, D., & Burns, M. (2018). UAV magnetometry for chromite exploration in the *Samail ophiolite* sequence Oman. *Journal of Unmanned Vehicle Systems, 6*(1), 57–69. https://doi.org/10.1139/juvs-2017-0015.

Pei, Y., Liu, B., Hua, Q., Liu, C., & Ji, Y. (2017). An aeromagnetic survey system based on an unmanned autonomous helicopter: Development, experiment, and analysis. *International Journal of Remote Sensing, 38*(8–10), 3068–3083. https://doi.org/10.1080/01431161.2016.1274448.

SIGEOM. (2020). Système d'information géominière du Québe. Accessed: 15 July 2020. http://sigeom.mines.gouv.qc.ca/

Sterligov, B., & Cherkasov, S. (2016). Reducing magnetic noise of an unmanned aerial vehicle for high-quality magnetic surveys. *International Journal of Geophysics, 2016,* 1–7. https://doi.org/10.1155/2016/4098275.

Sterligov, B., Cherkasov, S., Kapshtan, D., & Kurmaeva, V. (2018). An experimental aeromagnetic survey using a rubidium vapor magnetometer attached to the rotary-wings unmanned aerial vehicle. *First Break, 36*(1), 39–45.

Stoll, J. (2013). Unmanned aircraft systems for rapid near surface geophysical measurements. *The International Archives of the Photogrammetry, Remote Sensing and Spatial Information Sciences.* https://doi.org/10.5194/isprsarchives-XL-1-W2-391-2013.

Taner, M. F., & Chemam, M. (2015). Algoma-type banded iron formation (BIF), Abitibi Greenstone belt, Quebec, Canada. *Ore Geology Reviews, 70,* 31–46.

Tuck, L., Samson, C., Laliberté, J., Wells, M., & Bélanger, F. (2018). Magnetic interference testing method for an electric fixed-wing unmanned aircraft system (UAS). *Journal of Unmanned Vehicle Systems., 6,* 177–194. https://doi.org/10.1139/juvs-2018-0006.

Tuck, L., Samson, C., Polowick, C., & Laliberté, J. (2019). Real-time compensation of magnetic data acquired by a signle-rotor

unmanned aircraft system. *Geophysical Prospecting., 67,* 1637–1651. https://doi.org/10.1111/1365-2478.12800.

Vallée, M., Farquharson, C., Morrison, W., King, J., Byrne, K., Lesage, G., et al. (2019). Comparison of geophysical inversion programs run on aeromagnetic data collected over the Highland Valley Copper district, British Columbia Canada. *Exploration Geophysics., 50*(3), 310–323.

Walker, S. (2018). Sometimes innovative tools require an FAQ: lessons learned inverting magnetic data. *SEG Technical Program Expanded Abstracts.* https://doi.org/10.1190/segam2018-2998403.1.

Walter, C., Braun, A., & Fotopoulos, G. (2019a). High-resolution unmanned aerial vehicle aeromagnetic surveys for mineral exploration targets. *Geophysical Prospecting., 68,* 334–349. https://doi.org/10.1111/1365-2478.12914.

Walter, C., Braun, A., & Fotopoulos, G. (2019b). Spectral analysis of magnetometer swing in high-resolution UAV-borne aeromagnetic surveys. *IEEE Stratus.* https://doi.org/10.1109/stratus.2019.8713313.

Walter, C., Braun, A., & Fotopoulos, G. (2019c). Impact of three-dimensional attitude variations of an unmanned aerial vehicle magnetometry system on magnetic data quality. *Geophysical Prospecting., 67,* 465–479. https://doi.org/10.1111/1365-2478.12727.

Wood, A., Cook, I., Doyle, B., Cunningham, M., & Samson, C. (2016). Experimental aeromagnetic survey using an unmanned air system. *The Leading Edge, 35,* 270–273. https://doi.org/10.1190/tle35030270.1.